Christopher Cardenas[1]
e-mail: CVCardenas@gmail.com

Drazen Fabris

Shawn Tokairin

Department of Mechanical Engineering,
Santa Clara University,
500 El Camino Real,
Santa Clara, CA 95053;
Center for Nanostructures,
Santa Clara University,
500 El Camino Real,
Santa Clara, CA 95053

Francisco Madriz

Cary Y. Yang

Department of Electrical Engineering,
Santa Clara University,
500 El Camino Real,
Santa Clara, CA 95053;
Center for Nanostructures,
Santa Clara University,
500 El Camino Real,
Santa Clara, CA 95053

Thermoreflectance Measurement of Temperature and Thermal Resistance of Thin Film Gold

To improve performance and reliability of integrated circuits, accurate knowledge of thermal transport properties must be possessed. In particular, reduced dimensions increase boundary scattering and the significance of thermal contact resistance. A thermoreflectance measurement can be used with a valid heat transport model to experimentally quantify the contact thermal resistance of thin film interconnects. In the current work, a quasi-steady state thermoreflectance measurement is used to determine the temperature distribution of a thin film gold interconnect (100 nm) undergoing Joule heating. By comparing the data to a heat transport model accounting for thermal diffusion, dissipation, and Joule heating, a measure of the thermal dissipation or overall thermal resistance of unit area is obtained. The gold film to substrate overall thermal resistance of unit area beneath the wide lead (10 μm) and narrow line (1 μm) of the interconnect are 1.64×10^{-6} m^2 K/W *and* 5.94×10^{-6} m^2 K/W*, respectively. The thermal resistance of unit area measurements is comparable with published results based on a pump-probe thermoreflectance measurement.* [DOI: 10.1115/1.4007068]

Keywords: thin film, thermoreflectance, conduction thermal transport, joule heating, thermal resistance, microscale

Introduction

The performance of small scale integrated circuits relies on the understanding of the generation and transport of heat. At small scales, the electrical resistance increases due to reduction in grain size and increased boundary reflection [1,2]. This increase in resistance therefore leads to increased energy generation and inclination for thermal induced failure in circuits. Moreover, further improvements to reduce the scale of integrated circuits require understanding of the heat transfer for such systems [3–5]. Improvements in circuit and device design will depend on accurate experimental characterization of material properties and heat dissipation. Thermal induced failure is based on the local heating of structures and the ability to transfer heat to the substrate. The thermal resistance between the conductor and substrate can be material, geometry, and process dependent. Therefore, a direct measurement of local heating and thermal resistances are necessary [6,7].

In situ technical temperature measurement at a small scale poses challenges. There exist a number of specialized techniques for temperature measurement at small scales [8–10]. Noncontact techniques are often used to avoid significant contact loading and alteration of the thermal capacitance of the sample when measuring the local temperature. A thermoreflectance temperature measurement can utilize the temperature dependence of the normal reflectance intensity to measure the temperature [11–13]. The change in normal reflectance intensity due to change in temperature is small and can be linearized over a wide temperature range. The measurement is calibrated through definition of the thermoreflectance coefficient, κ ($^\circ C^{-1}$)

$$\kappa = \frac{1}{I_0}\frac{\partial I_n}{\partial T} \tag{1}$$

$$I_n = I_0 + \kappa(T - T_0)I_0 \tag{2}$$

where I_n (A.U.) is the normal reflectance intensity at elevated temperature T (°C) and I_0 (A.U.) is the normal reflectance intensity at the reference temperature T_0. With calibration of a material's thermoreflectance coefficient in the normal direction, the temperature difference can then be measured by Eq. (2).

The measurement technique has been shown capable of providing a measure of the wide-field temperature difference distribution from the far field down to the diffraction limit of the optics [10]. The thermal measurement accuracy is governed by the material thermoreflectance sensitivity, which is wavelength dependent, resolution of reflectance sensing equipment, and extent of the time and spatial averaging utilized. It has been shown that thermal accuracy can achieve 10 mK and spatial resolution typically approaches 230 nm [14,15]. The advantages of this technique and the developed thermoreflectance apparatus are the simplicity of the experimental setup, negligible biasing, and the accuracy of the final measurement.

This work demonstrates the use of the thermoreflectance technique to measure the temperature difference field of a model gold line interconnect system. A substantial temperature gradient during Joule heating of the structure occurs along a thin (100 nm) and narrow (1 μm) line. Following the temperature difference measurement, the data are used to determine the overall thermal resistance of unit area to the substrate by comparison with a 2D steady state heat transport model of the system.

[1]Corresponding author.

Contributed by the Heat Transfer Division of ASME for publication in the JOURNAL OF HEAT TRANSFER. Manuscript received May 16, 2011; final manuscript received May 28, 2012; published online September 26, 2012. Assoc. Editor: Kenneth Goodson.

The reliability of these interconnects is governed by conduction of heat to the substrate during Joule heating. Assuming 1D conduction heat transfer to the substrate, a thermal resistance analogy is possible. By this method, the ratio of the local temperature difference to the local heat flux fundamentally defines the overall thermal resistance of unit area

$$\dot{q}'' = \left(\frac{1}{\Sigma R''}\right)\Delta T \tag{3}$$

where $\Sigma R''$ (m^2 K/W) is the overall thermal resistance of unit area. The overall thermal resistance of unit area is further defined by the sum of all contributions to the quantity

$$\Sigma R'' = \Sigma R''_c + \Sigma R''_{\text{Bulk}} \tag{4}$$

where $\Sigma R''_c$ refers to the sum of contact resistances between deposited film layers and $\Sigma R''_{\text{Bulk}}$ refers to the sum of thickness dependent conduction resistances of each layer. For a single layer with thickness, t, the thermal resistance of unit area is inversely proportional to the thermal conductivity, $R''_{\text{Bulk}} = t/k$. For the assumption to hold, temperature into the substrate linearly varies with depth. At interfaces, there is an abrupt change in temperature due to contact thermal resistance, R''_c.

The contact thermal resistance can be due to void formation at the bimaterial interface, acoustic mismatch between the phonon propagation velocity, and the phonon distribution in the bimaterial interface. In thin layers (~100 nm), the thermal conductivity should be affected by confinement, surface conditions, temperature, internal structure, and impurities in the material. Overall thermal resistance is typically dominated by the contact resistances of interfaces for such thin films. This is supported by the research of Burzo et al. [16] which showed a large contribution from the sum of layer to layer contact resistances, $\Sigma R''_c \sim (0.78\text{–}2.58) \times 10^{-8}$ m^2 K/W. In similar work, Pop used thermal conductance to determine the temperature in carbon nanotubes [17]. In selected interface applications, it is common to encounter larger contact thermal resistances of unit area, $R''_c \sim (0.01\text{–}25) \times 10^{-4}$ m^2 K/W [18]. As thickness of the supporting insulation increases, layer specific thermal resistance is expected to increase beyond the contact thermal resistance term. Hence, a technique that can measure two-dimensional temperature fields and determine the overall thermal resistance to the substrate will be useful for assessing circuit reliability for emerging technologies [19].

Reflectance is dependent on the complex refractive index of materials and mediums and is well understood from both theory and measurement [20,21]. Temperature dependence of optical reflectance has also been well understood for some time [11,22]. Gold optical properties and the temperature dependences are available in literature to support thermoreflectance measurements.

Experiments

The samples consist of model thin film interconnects constructed of gold. Gold was chosen as a material due to inertness, the possibility for use in other applications, and use in parallel research [23]. The interconnect test structures were originally designed for a transmission line measurement and were also able to be utilized for thermoreflectance experiments.

The interconnect substrate consists of several layers (Fig. 1). The substrate stack from lowest to top is composed of a silicon wafer followed by a deposited amorphous SiO_2 insulation layer with a 10 nm titanium adhesion layer in contact with the gold. The interconnect layout consist of two pads used for landing low impedance electrical probes, thin film leads, and a narrow test line connecting the leads. Fabrication of the line length was systematically varied from 1 to 50 μm. Data contained in this work are gathered on a line of 20 μm in length.

The increase of electrical resistivity is to be expected due to the small thickness of the film. In metals, the ratio of thermal

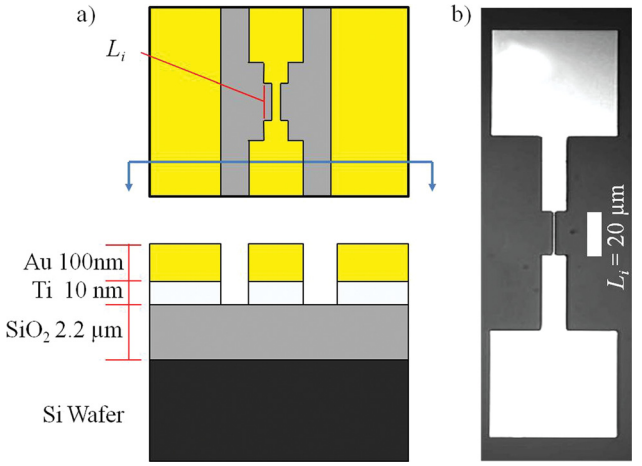

Fig. 1 Thin gold film sample (*a*) schematic of layered deposition (*b*) microscope image

conductivity to electrical conductivity is governed by the Wiedemann–Franz law [24]. The thermal conductivity in metals is generally driven by electron transport. Electrical properties for the gold were measured with a Cascade Microtech® probe station and analyzer. The sheet resistance of the gold film at room temperature, $1/(t_{Au}\sigma_{Au})|_{T=20\,^\circ\text{C}}$, was found to be 0.392 ± 8% Ω/sq, a 72% increase from the bulk value. Thus, a measurement of electrical resistivity can be used to estimate the change of thermal conductivity from the bulk value, $k_{Au}|_{T=20\,^\circ\text{C}} \sim 317/1.61 = 197$ W/m K.

The in-plane thermal conductivity of the gold film was estimated from the change in electrical conductivity. This thermal conductivity is used to determine the in-plane conduction relative to the heat transport to the substrate. Researchers have determined gold thin film properties by surface laser heating and a system transient response. In one work, the thermal conductivity of a thin film gold has been shown to decrease with thickness from 315 to 190 W/m K for 1750–600 nm thin films [25]. While in another, the thermal conductivity reduces from 320 to 100 W/m K for 2000 to 100 nm thin films [26]. The current work differs in that the heating is applied throughout the bulk of thin film via Joule heating and that the time scale (0.1 s) also assures that a quasi-steady thermal profile is established. Under this type of heating, the gold film can be accurately approximated as nearly isothermal across its thickness. The variation in temperature across the gold film scales with the ratio of its thickness to thermal conductivity relative to the thickness to thermal conductivity of the substrate. Therefore, the thermal transport to the substrate is based on a local gold temperature that is the same at the gold/Ti interface and the film surface and the measurement is not sensitive to the thermal conductivity across the film.

The thermoreflectance apparatus is shown in Fig. 2. It consists of a high power optical microscope, a heated sample holder, electrical probes, a light emitting diode (LED), a charge-couple device (CCD), probe station, and acquisition equipment. The objective lens is a Meiji Techno MA921. The samples are interrogated with Philips LUXEON® Star/O LED illumination. These LED models are currently discontinued. Measurements of film temperature with the calibration thermocouple placed in the vicinity of the imaged area while using the same optic setup used during this work confirmed that there was no significant (<1 °C) temperature change when LED light illuminated the surface. The LED characteristics indicating the manufacturer specified peak emission wavelength, $\lambda_{\text{Peak,Manu.}}$, measured peak wavelength, λ_{LED}, and spectral line half width, $\Delta\lambda_{1/2}$, can be found in Table 1. LED spectral emission distributions were measured with an Ocean Optics USB 2000 spectrometer in place at the location of samples.

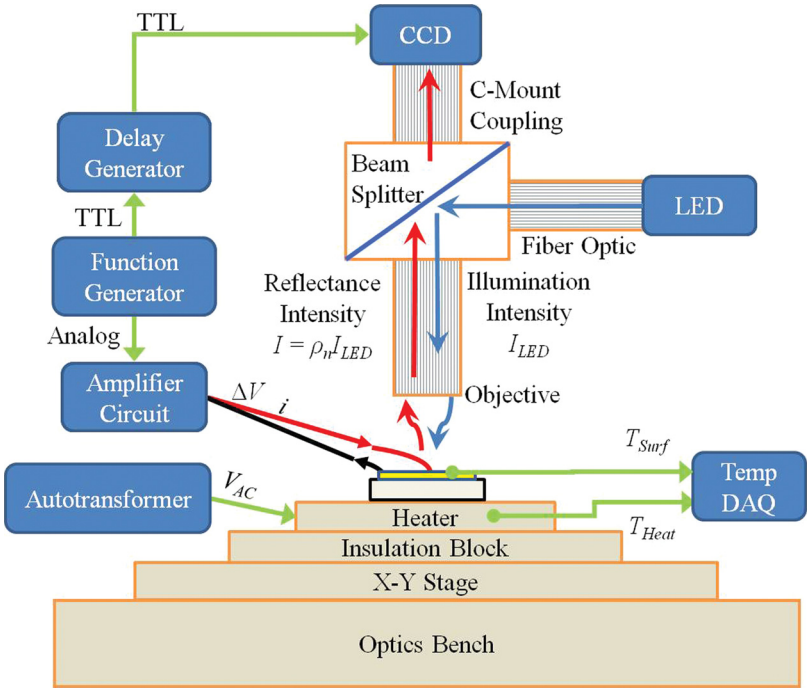

Fig. 2 Thermoreflectance system schematic diagram with hardware components

The reflectance intensity images are captured with a 12-bit A/D CCD camera (Prosilica GE1380). The experimental apparatus has a custom built heated stage with micrometers used for manual controlled positioning. The entire system is placed on an optical table to reduce vibrations.

The experiments consist of capturing a consecutive series of images while a square wave voltage signal is applied to the sample. The square wave heating signal and CCD timing are generated by a function generator. The square analog output is half wave rectified, amplified by an op-amp circuit, and passed through the sample while simultaneously measuring the current drawn. The timing signal is delivered to a delay generator for lock-in image acquisition at twice the heating frequency. A series of hot and relaxed images are then acquired and later separated according to frame parity. The time sequence of the data capture is shown in Fig. 3. Since the structures are very small, the transient heating time is very short and the system is in a quasi-steady state (transient time is estimated to be less than 25 ms). The experiments were run at several current values to vary the amount of energy generation.

During the experimental measurement, acquisition of repeated hot and relaxed sample images acts to average the long-time fluctuations in the illumination and other environmental variables. In the end, the ability to accurately measure the temperature difference is based on the capacity to measure the temperature dependent relative changes in reflectance down to nearly 2/10th of a percent ($\kappa \sim -2 \times 10^{-4}\,^{\circ}\mathrm{C}^{-1}$) under $\lambda_{LED} = 530$ nm. Acquisition of measurement data are typically achieved for 4000 total frames over the duration of several minutes.

The thermoreflectance calibration coefficient is not widely available in literature and possible underlying causes of variations necessitate calibrations for the samples to be tested. Variations in the calibration coefficient may arise from, but are not limited to: film thicknesses, light source emission spectrum variations due to laboratory temperature changes, optical components, CCD sensitivity, material surface conditions, and material purity. In the calibration and experiments conducted, the 100 nm thin gold film is not expected to show substantial thermal expansion, but any contribution is systematically captured in the measurements [27]. Calibration and measurements are performed in an open air laboratory environment. Calibrations were performed using the four LED's described and results are compared with two data sets

Table 1 Manufacturer model number of LED corresponding with the manufacturer specified peak emission wavelength ($\lambda_{Peak,Manu.}$), measured peak emission wavelength (λ_{LED}), and spectral line half width ($\Delta\lambda_{1/2}$)

Model number	$\lambda_{Peak,Manu.}$ (nm)	λ_{LED} (nm)	$\Delta\lambda_{1/2,Meas.}$ (nm)
LXHL-NRR8	455	446	26
LXHL-NB98	470	458	26
LXHL-NE98	505	494	26
LXHL-NM98	530	535	31

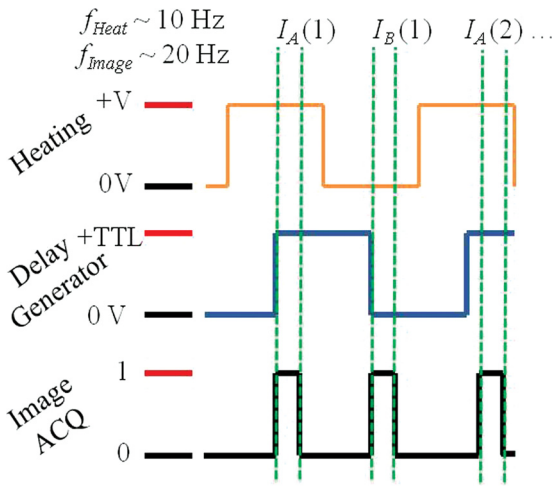

Fig. 3 Heating, delay, and image acquisition timing signals for quasi-steady lock-in thermoreflectance imaging. Low power LED illumination is constant. I_A and I_B refer to heated and cooled reflectance intensity images, respectively.

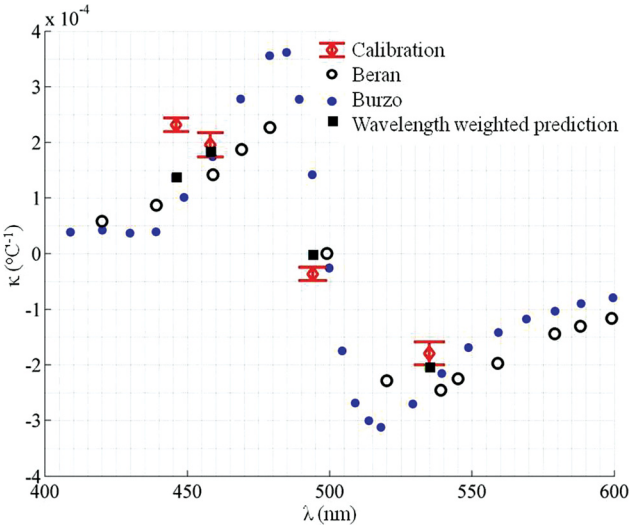

Fig. 4 Thermoreflectance calibration under LED illumination. Data from Refs. [28] and [29] are included for comparison of results for similar techniques on similar structures.

of experimentally acquired published data for gold (Fig. 4). During the calibration, the sample is first heated to beyond 200 °C and then progressively cooled. Thermoreflectance data are reproduced and repeatable only for decreasing and cycling temperature from the peak temperature during calibration, 200 °C down to ambient. Measurements are taken at multiple steady state temperatures during the cooling and heating. The heated sample stage enables fixed temperature control to achieve a thermal steady state (±0.3 °C). Surface temperature was measured with a small surface deposited thermocouple, wire diameter <13 μm. Following acquisition, the thermoreflectance coefficient was then calculated by use of Eqs. (1) and (2).

Calibration beyond 250 °C was not possible since delamination of the gold film occurred and the peal temperature was therefore limited to 200 °C to prevent possible damage. After the initial cycle where an adsorbed layer is evaporated, the thermoreflectance coefficient showed consistent values. With three repeated measurements under LED illumination with a peak wavelength of 535 nm, the average value of the calibration coefficient was -1.71×10^{-4} ($^{\circ}C^{-1}$) with a standard deviation of 0.19×10^{-4} ($^{\circ}C^{-1}$). Due to the time required to stabilize the temperature and collect stable reflectance intensity data only four temperatures are used in the calibration. The linear fit used to determine the reflectance coefficient has a correlation coefficient of 0.9937; therefore, it is reasonable to use a constant thermoreflectance coefficient value over the measured temperature range with a ±15% confidence in the value. Thermally induced spatial displacements are determined by image detection of edges and are manually corrected. Unlike previously reported [15], average reflectance intensity by CCD measurement show linear proportionality to objective distance from the surface.

The data show good agreement to the two published measurements [28,29] in Fig. 4. Wavelength weighted predictions of the thermoreflectance calibration coefficients have been included for comparison to the data. The weighted average computation, discussed in Ref. [19], utilizes the spectral sensitivity of the CCD, illumination distribution of each LED, and the laser based calibration reported in Ref. [29] to predict the quantity under LED specific illumination. Compared to the laser based method, the data demonstrate the correct trend with a decrease in the magnitude due to the spectral width of the LEDs and CCD readout sensitivity. The method reported by Beran made use of a monochromator bandwidth of 6 nm reducing the spectral averaging and more closely matching the data of Burzo. Uncertainty in the thermoreflectance coefficient of gold is measured with 95% confidence

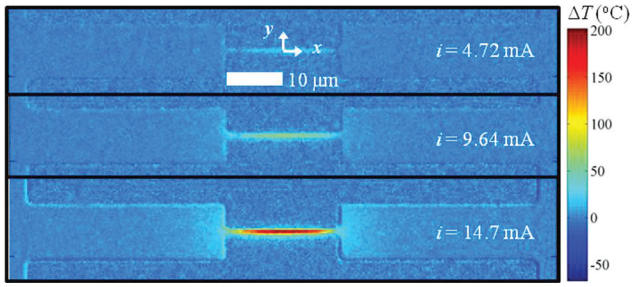

Fig. 5 2D temperature difference measurement during quasi-steady increase of Joule heating in the structure under $\lambda_{LED} = 535$ nm

based on the variation in the collected data. Significant contributions to systematic error include uncertainty in the thermocouple temperature measurement (<0.3 °C), local spatial variation of intensity (<0.12%), and repeated mean intensity variation (<0.76%). The overall uncertainty in the thermoreflectance calibration coefficient under LED illumination is ±15%.

We have characterized hysteresis of the metallic thermoreflectance calibration with increasing and decreasing sample temperature and measuring data in time following thermal cycling of the samples. The hysteresis is believed to be due to water adsorption at the surface [30]. The water is removed when the sample is heated above the vaporization temperature. Under some illumination wavelengths, the hysteresis is minimal, but under others the sign of the thermoreflectance calibration coefficient may change [31]. Repeatable thermoreflectance has been measured during the decrease and repeated cycling of the sample temperature and is nearly a reproduction of the spectrally weighted published thermoreflectance calibration data [29].

Results

Temperature difference fields for increasing current are shown in Fig. 5. The data show high heating of the gold structure in the narrow line and lesser heating in the lead where the width is expanded. This corresponds to the higher current density in the narrow line. The signal gradients show strong 1D temperature distribution from the center segment, 2D behavior in the transition region, and approach to 1D in the extent of the lead where the signal approaches the noise level of the measurement. The noise level of averaged pixel to pixel readout produces an uncertainty of 10 C. The random noise is due to variation in the pixel readout, illumination, microscale vibration, and the need for high sensitivity in the measurement. This noise level may be improved by acquisition of more images and improving the uncertainty of the calibration coefficient. The data exhibit high symmetry at the midpoint and along the centerline. The appearance of edges is explained by false relative reflectance shifting induced from lateral vibration during the imaging. The amplitude of the lateral vibration is less than 2 pixels.

Comparisons of the centerline experimental data to 2D thermal model solutions are shown in Fig. 6. The data shown are acquired from the subspace in the image along the center of the gold line ($-20 \leq x \leq 20$ μm and $y = 0$ μm). The experimental data are compared to a 2D steady state thermal model accounting for diffusion, conduction heat transfer to the substrate, and Joule heating.

$$\left(\frac{\partial^2 \Delta T}{\partial x^2} + \frac{\partial^2 \Delta T}{\partial y^2}\right) - a^2 \Delta T = -bJ^2 \tag{5}$$

where $\Delta T(x,y)$ is the local temperature difference (°C), J is the current density (A/m^2), a is the thermal dissipation factor (m^{-1}), and b is the constant defined by the inverse product of the electrical conductivity and thermal conductivity, $b = (\sigma_{Au} k_{Au})^{-1}$.

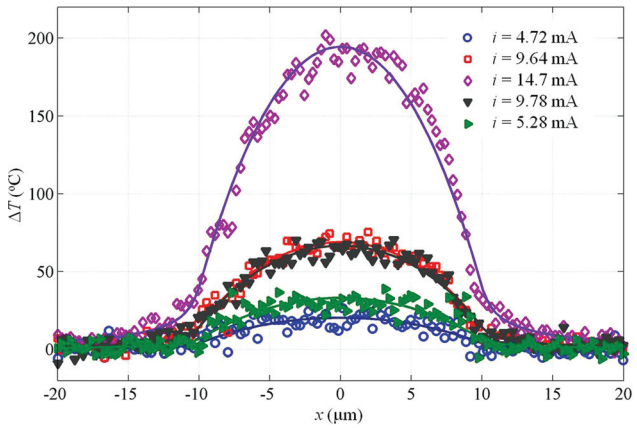

Fig. 6 Temperature profile data ($\lambda_{LED} = 535$ nm) with best-fit 2D model solutions (solid lines). Repeated measurements were performed at the lower current levels.

The second order inhomogeneous elliptic partial differential equation (screened Poisson) is solved by a finite difference method. Based on the symmetry of the data, we model a quadrant of the gold thin film with Eq. (5). The boundary conditions of the quadrant were treated with adiabatic/symmetric walls and prescribed temperature at the extent of the leads, Table 2.

In this formulation, the following assumptions were made: 2D heat transfer in the plane of the film, 1D conductive heat transfer to the substrate lumped in the dissipation factor a, constant thermal and electrical properties, isotropic thermal conductivity, uniform current density, and reduced transport conductivities from bulk properties for measured σ_{Au} and estimated k_{Au}.

The data are well represented by the 2D model solutions (Fig. 6) in both the narrow region of maximum heating and the expansion to the lead. The thermal dissipation factor a accounts for the overall heat transfer from the conductor which is dominated by conduction heat transfer to the substrate. This model applied to the system allows for treatment with two piecewise constant values of current density and the thermal dissipation. Below the narrow line (a_i where $0 \le x \le 10$ μm) and the lead (a_o where $10 < x \le 45$ μm) local thermal dissipation, similar to a local convective heat transfer coefficient, quantifies the heat transfer to the substrate. To obtain the best fit, the modeled centerline solution is least squares fit to the centerline of the experimental data by adjusting the thermal dissipation factors (a_i and a_o). Validation of the finite difference method solution of the model was performed by comparison to a commercial code. The error between the commercial solution and the finite difference method solution was less than 1 °C at the maximum heating point ($x = 0$ and $y = 0$) for maximum heating conditions ($i = 15$ mA). Contained in Table 3, are the thermal dissipation values from fitting the model to the data with the calculated mean and confidence interval of the means to 95%. The 2D modeled temperature field is more sensitive to the dissipation factor imposed in the narrow line region rather than in the lead region, hence larger uncertainty intervals of the means are acquired in this section.

The 2D model solutions are compared with a simplified model developed for similar 1D systems [32–34]. The model previously presented is the 1D simplification of the model proposed in this work which is applicable when temperature dependence in y can be neglected, i.e., $\partial^2 \Delta T / \partial y^2 = 0$. Similarly the model applied on the system allows for piecewise variation in the conductor geometry, current density, and conduction to the substrate. Likewise, the 1D model solutions are fit to the data in the least squared sense to obtain the best fitting thermal dissipation values (Table 3). To obtain a full 1D analytic solution four boundary conditions are needed, which are defined by the measurement data characteristics: symmetry at the midpoint, continuous temperature at the junction, constant heat rate at the junction, and fixed ambient temperature at extent of the leads. The 1D solution approaches the centerline temperature distribution of the 2D data and model solution (Fig. 7). The measurement data and 2D model exhibit the spreading of heat flux lines and an increase in temperature in the junction and narrow region. These are physical characteristics that the full 1D solution cannot capture without correction. Therefore, the best fitting thermal dissipation values by 1D modeling are systematically lower than the 2D inferred values (Table 3).

Table 2 Boundary condition treatment at edges of gold thin film structure

	Location	
Condition and quantity	x (μm)	y (μm)
$\dot{q}(x,y) = 0$ W	$x = 0$	$0 \le y \le 0.5$
$\dot{q}(x,y) = 0$ W	$0 \le x \le 10$	$y = 0.5$
$\dot{q}(x,y) = 0$ W	$x = 10$	$0.5 \le y \le 5$
$\dot{q}(x,y) = 0$ W	$10 \le x \le 45$	$y = 5$
$\dot{q}(x,y) = 0$ W	$0 \le x \le 45$	$y = 0$
$\Delta T(x,y) = 0$ °C	$x = 45$	$0 \le y \le 5$

Discussion

To compare with existing data, conversion to the overall thermal resistance must be performed. A direct conversion to the overall thermal resistance from the thermal dissipation factor, invoked in Eq. (5), is performed by again considering the heat flux to the substrate in Eq. (2)

$$\dot{q}'' = \left(\frac{1}{\Sigma R''}\right)\Delta T = \left(a^2 k_{Au} t_{Au}\right)\Delta T \tag{6a}$$

$$\Sigma R'' = \left(a^2 k_{Au} t_{Au}\right)^{-1} \tag{6b}$$

The overall thermal resistance of gold deposited on SiO_2 substrates has been studied with inclusion or deduction of a chromium adhesion layer. Within that research, both ion beam sputtered (IBS) and thermally grown (TG) SiO_2 were used [16]. Thicknesses of the SiO_2 were varied to acquire the contact contribution to the overall thermal resistance of unit area. It had been reported that over the range of SiO_2 thickness (100–1000 Å) the thermal conductivity shows weak thickness dependence from the SiO_2 and the thermal conductivity measured is smaller than the bulk value for both IBS and TG material. A similar sample

Table 3 Experimental measurements and fit thermal dissipation values a for the inner gold line a_i and wider lead a_o

i (mA)	$a_i \times 10^5$ (m^{-1})	$a_o \times 10^5$ (m^{-1})
$\lambda_{LED} = 535$ nm (2D model)		
4.72	0.90	2.04
9.64	1.20	1.87
14.7	0.93	1.74
9.78	1.29	1.80
5.28	0.46	1.64
$\bar{a}$	0.96	1.82
$(+/-)_{Mean(95\%)}$	0.40	0.19
$\lambda_{LED} = 535$ nm (1D model)		
4.72	0.78	1.72
9.64	1.11	1.64
14.7	0.80	1.40
9.78	1.20	1.60
5.28	0.10	1.33
$\bar{a}$	0.80	1.54
$(+/-)_{Mean(95\%)}$	0.53	0.20

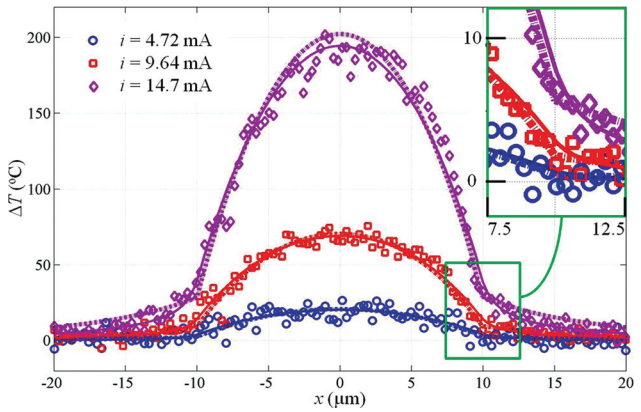

Fig. 7 Temperature profile data with 2D model fitting (solid lines) and 1D model fitting (dotted lines)

configuration is presented in this work to the thermally grown SiO_2 with a Cr adhesion layer. Validation of the current measurements is performed by extrapolating the literature data. The converted data are contained in Table 4.

An extrapolation from the published data predicts a thermal resistance through the SiO_2 layer of $1.74 \times 10^{-6} \pm 3\%$ m^2 K/W. This value is obtained by using the reported fit for the similar sample configuration with the thickness of the SiO_2 used in the current research, $\Sigma R'' = (0.787)$ m K/W $\times (2.2 \times 10^{-6})$ m $+ 0.78 \times 10^{-8}$ m^2 K/W [16]. Utilizing the dominant thermal resistance as that of the SiO_2 layer with the bulk thermal conductivity (1.4 W/m K) one may calculate 1.6×10^{-6} m^2 K/W for our setup. This thermal resistance of the oxide layer is substantially higher than the contact thermal resistance from the gold to the oxide, 1.8×10^{-8} m^2 K/W [35]. Thus, our data approach agreement with the reported and bulk dominant value. The increase in overall thermal resistance of unit area under the narrow line occurs because of an increase in thermal contact resistance possibly due to thermal expansion, increased scattering, and/or variation in the fabrication of the thin film. Full 3D numerical results have shown that to achieve the measured temperature at the midpoint and a parabolic local temperature profile, a significant contact resistance on the order of the overall thermal resistance beneath the narrow line is required [19,32]. Insufficient data were collected to inspect the temperature dependence of the thermal contact resistance.

Reflectance intensity measurements have indicated that diffraction occurs at the edges of the Au film transitioning into the surrounding region. The size of the diffraction patterns measured is on the order of the narrow 1 μm line. The resulting reflectance intensity profiles are dependent on the diffraction process which in turn is dependent on the wavelengths investigated, structure sizes under interrogation, and the magnitudes of the reflectance over regions of materials, Au and SiO_2. Improved reflectance intensity signals for gold are possible at longer wavelengths of light [28]. Our data show that over large regions the ratio of surrounding to Au reflectance, ρ_{SiO_2}/ρ_{Au}, decreases from 1.00 to 0.38 for λ_{LED} from 446 nm to 535 nm, respectively. Therefore, due to the weaker reflectance for gold and poor contrast with the surrounding signal at shorter wavelengths than 500 nm diffractive effects lead to inaccurate results when applying current calibration data to convert the relative reflectance signal to a temperature difference signal.

Table 4 Fit thermal dissipation and conversion to overall thermal resistance of unit area

	$\lambda_{LED} = 535$ nm	
(2D model)	Line	Lead
$\bar{a} \times 10^5$ (m^{-1})	0.96	1.82
$(+/-)_{Mean(95\%)}$	0.40	0.19
$\sum R'' \times 10^{-6}$ (m^2 K/W)	5.94	1.64
$(+/-)_{Mean(95\%)}$	3.00	0.29

The current magnitude of the inferred data, $\Sigma R''$, show good agreement to the values obtained by a concomitant measurement and the dominant bulk value calculation for our setup which supports the presented measurements under $\lambda_{LED} = 535$ nm. We are currently working on a model to better understand the previously mentioned effects due to diffraction. With this model, further measurements at different wavelengths will help to understand the accuracy of the technique for measurements at smaller spatial scales.

Several distinctions are apparent in the current method compared to prior work. The method utilizes Joule heat generation as opposed to laser pump heating thus being a minimally invasive method and an in situ measurement of the self heating. The CCD allows for a simultaneous measurement of the 2D temperature field. Application of the measurement technique in combination with the numerical model allows for the measurement of the overall thermal resistance of unit area for a metallic interconnect while in quasi-steady operation. Pump-probe measurements will continue to show temporal speed advantage beyond the capability of wide view measurements. This is an essential requirement of an experiment to assess in situ performance of circuitry, but the spatial resolutions are nearly equivalent.

Conclusions

We have demonstrated utilization of the thermoreflectance technique to acquire temperature difference measurements of self-heating gold thin film structures. The current thermal and spatial resolutions of the measurement are reported at $\pm 10\,^{\circ}$C and 314 nm, respectively. Thermoreflectance calibration values reported are consistent to literature values following heating to 200 °C to avoid hysteresis. The apparatus presented is a much simplified experimental setup from other methods which provide the measurements needed to determine transport properties for the structures tested.

Modeling of the measured temperature distributions was performed by solving the 2D heat transport model proposed. It has been shown that a 2D model of the system is sufficient to fully describe the temperature difference field. A simplified full 1D model under predicts the temperature distributions for constant properties which leads to the systematic decrease of the best fitting thermal dissipation values.

In the present work, overall thermal resistance of unit area beneath the piecewise treated gold thin film structure has been reported. Although single sample geometry limits the determination of thermal resistance to the overall sum of contact and layer thermal resistances, the data compare well to existing research and the dominant value calculation therefore validating the current methods. Below the heated section, the results show an increase in thermal resistance of unit area.

Acknowledgment

This work was supported by the United States Army Space and Missile Defense Command (SMDC) and carries Distribution Statement A, approved for public release, distribution unlimited.

Nomenclature

I = reflectance intensity, arbitrary units or A.U.
J = current density, A/m^2
L = length, m
R'' = thermal resistance of unit area, m^2 K/W
T = temperature, °C
V = voltage, V

a = thermal dissipation, m^{-1}
f = frequency, Hz
i = electric current, A
k = thermal conductivity, W/(m K)
$\dot{q}$ = heat rate, W
$\dot{q}''$ = heat flux, W/m^2
t = thickness, m
x = spatial dimension, m
y = spatial dimension, m

Greek Symbols

κ = thermoreflectance calibration coefficient, $°C^{-1}$
λ = wavelength, nm
ρ = reflectance
σ = electrical conductivity, $(\Omega\text{-m})^{-1}$

Subscripts

0 = reference quantity
AC = alternating current property
Heat = heater quantity
i = internal section of interconnect or along narrow structure
Image = imaging property
LED = light emitting diode property
n = normal direction
o = outer section of interconnect or along wider lead section
Peak = peak of emission
Surf = surface quantity

References

[1] Flik, M. I., Choi, B. I., and Goodson, K. E., 1992, "Heat Transfer Regimes in Microstructures," ASME J. Heat Transfer, **114**, pp. 666–674.
[2] Shakouri, A., 2006, "Nanoscale Thermal Transport and Microrefrigerators on a Chip," Proc. IEEE, **94**(8), pp. 1613–1638.
[3] Chen, G., 2006, "Nanoscale Heat Transfer and Nanostructured Thermoelectrics," IEEE Trans. Compon. Packag. Technol., **29**(2), pp. 238–246.
[4] Pop, E., 2010, "Energy Dissipation and Transport in Nanoscale Devices," Nano Res., **3**, pp. 147–169.
[5] Cahill, D. G., Ford, W. K., Goodson, K. E., Mahan, G. D., Majumdar, A., Maris, H. J., Merlin, R., and Phillpot, S. R., 2003, "Nanoscale Thermal Transport," J. Appl. Phys., **93**(2), pp. 793–818.
[6] Pop, E., and Goodson, K. E., 2006, "Thermal Phenomena in Nanoscale Transistors," ASME J. Electron. Packag., **128**, pp. 102–108.
[7] Burzo, M. G., Komarov, P. L., and Raad, P. E., 2005, "Noncontact Transient Temperature Mapping of Active Electronic Devices Using the Thermoreflectance Method," IEEE Trans. Compon. Packag. Technol., **28**(4), pp. 637–643.
[8] Cahill, D. G., Goodson, K., and Majumdar, A., 2002, "Thermometry and Thermal Transport in Micro/Nanoscale Solid-State Devices and Structures," ASME J. Heat Transfer, **124**, pp. 223–241.
[9] Altet, J., Claeys, W., Dilhaire, S., and Rubio, A., 2006, "Dynamic Surface Temperature Measurements in ICs," Proc. IEEE, **94**(8), pp. 1519–1533.
[10] Christofferson, J., Maize, K., Ezzahri, Y., Shabani, J., Wang, X., and Shakouri, A., 2007, "Microscale and Nanoscale Thermal Characterization Techniques," Thermal Issues in Emerging Technologies, THETA 1, Cairo, Egypt, pp. 3–9.
[11] Farzaneh, M., Maize, K., Lüerßen, D., Summers, J. A., Mayer, P. M., Raad, P. E., Pipe, K. P., Shakouri, A., Ram, R. J., and Hudgings, J. A., 2009, "CCD-Based Thermoreflectance Microscopy: Principles and Applications," J. Phys. D: Appl. Phys., **42**, p. 143001.
[12] Grauby, S., Forget, B. C., Holé, S., and Fournier, D., 1999, "High Resolution Photothermal Imaging of High Frequency Phenomena Using a Visible Charge Coupled Device Camera Associated With a Multichannel Lock-In Scheme," Rev. Sci. Instrum., **70**(9), pp. 3603–3608.
[13] Tessier, G., Holé, S., and Fournier, D., 2001, "Quantitative Thermal Imaging by Synchronous Thermoreflectance With Optimized Illumination Wavelengths," Appl. Phys. Lett., **78**(16), pp. 2267–2269.
[14] Lüerßen, D., Hudgings, J. A., Mayer, P. M., and Ram, R. J., 2005, "Nanoscale Thermoreflectance With 10mK Temperature Resolution Using Stochastic Resonance," 21st IEEE SEMI-THERM Symposium, San Jose, CA.
[15] Dilhaire, S., Grauby, S., and Claeys, W., 2003, "Calibration Procedure for Temperature Measurements by Thermoreflectance Under High Magnification Conditions," Appl. Phys. Lett., **84**(5), pp. 822–824.
[16] Burzo, M. G., Komarov, P. L., and Raad, P. E., 2003, "Thermal Transport Properties of Gold-Covered Thin-Film Silicon Dioxide," IEEE Trans. Compon. Packag. Technol., **26**(1), pp. 80–88.
[17] Pop, E., Mann, D. A., Goodson, K. E., and Dai, H., 2007, "Electrical and Thermal Transport in Metallic Single-Wall Carbon Nanotubes on Insulating Substrates," J. Appl. Phys., **101**, pp. 1–10.
[18] Incropera, F. P., DeWitt, D. P., Bergman, T. L., and Lavine, A. S., 2007, *Fundamentals of Heat and Mass Transfer*, John Wiley & Sons, Hoboken, NJ.
[19] Cardenas, C. V., 2011, "Thermoreflectance Temperature Measurement and Application to Gold Thin Films and Carbon Nanofibers," M.S. thesis, Department of Mechanical Engineering, Santa Clara University, Santa Clara, CA.
[20] Loebich, O., 1972, "The Optical Properties of Gold," Gold Bull., **5**(1), pp. 2–10.
[21] Lee, W., Kim, J. E., Park, H. Y., Park, S., Kim, M., Kim, J. T., and Ju, J. J., 2008, "Optical Constants of Evaporated Gold Thin Films Measured by Surface Plasmon Resonance at Telecommunication Wavelengths," J. Appl. Phys., **103**, p. 073713.
[22] Winsemius, P., van Kampen, F. F., Lengkeek, H. P., and van Went, C. G., 1976, "Temperature Dependence of the Optical Properties of Au, Ag, and Cu," J. Phys. F: Metal Phys., **6**(8), pp. 1583–1606.
[23] Madriz, F. R., Jameson, J. R., Krishnan, S., Sun, X., and Yang, C. Y., 2009, "Circuit Modeling of High-Frequency Electrical Conduction in Carbon Nanofibers," IEEE Trans. Electron Devices, **56**(8), pp. 1557–1561.
[24] Jones, W., and March, N. H., 1985, *Theoretical Solid State Physics: Non-Equilibrium and Disorder*, Vol. 2, Dover Publications, Mineola, NY, Chap. 6.12.
[25] Langer, G., and Hartmann, J., 1997, "Thermal Conductivity of Thin Film Metallic Films Measured by Photothermal Profile Analysis," Rev. Sci. Instrum., **68**(3), pp. 1510–1513.
[26] Bourgoin, J., Allogho, G., and Haché, A., 2010, "Thermal Conduction in Thin Films Measured by Optical Surface Thermal Lensing," J. Appl. Phys., **108**, p. 073520.
[27] Liu, Y., Mandelis, A., Choy, M., Wang, C., and Segal, L., 2005, "Remote Quantitative Temperature and Thickness Measurements of Plasma-Deposited Titanium Nitride Thin Coatings on Steel Using a Laser Interferometric Thermoreflectance Optical Thermometer," Rev. Sci. Instrum., **76**, p. 084902.
[28] Beran, A., 1985, "The Reflectance Behaviour of Gold at Temperatures up to 500 °C," Tschermaks Min. Petr. Mitt., **34**, pp. 211–215.
[29] Burzo, M. G., Komarov, P. L., and Raad, P. E., 2006, "Optimized Thermo-Reflectance System for Measuring the Thermal Properties of Thin-Films and Their Interfaces," 22nd Annual IEEE SEMI-THERM Symposium, pp. 87–94.
[30] Lee, S., and Staehle, R. W., 1996, "Study of Water Adsorbed on Gold: Assessment of Polarization Model," Material Transactions, J.I.M., **37**(12), pp. 1768–1773.
[31] Fabris, D., Cardenas, C., Tokairin, S., Wilhite, P., and Yang, C. Y., 2012, "Thermoreflectance Small Scale Temperature Measurement Under Ambient Conditions," 9th International Conference on Heat Transfer, Fluid Mechanics and Thermodynamics, HEFAT 2012, Malta.
[32] Fabris, D., Kitsuki, H., Yamada, T., Sun, X., Yang, C. Y., and Cruz, J. G., 2008, "Temperature Modeling for Carbon Nanofiber Breakdown," Proceedings of the 2008 ASME Summer Heat Transfer Conference, Jacksonville, FL, ASME Paper No. HT2008-56244.
[33] Fabris, D., Saito, T., Yamada, T., Sun, X., Wilhite, P., and Yang, C.Y., 2009, "Current Capacity and Thermal Transport in Carbon Nanofiber Interconnects," Proceedings of the 4th IEEE International Conference on Nano/Micro Engineered and Molecular Systems, Shenzhen, China, pp. 829–834.
[34] Yamada, T., Saito, T., Fabris, D., and Yang, C. Y., 2009, "Electrothermal Analysis of Breakdown in Carbon Nanofiber Interconnects," IEEE Electron Device Lett., **30**(5), pp. 469–471.
[35] Smith, A. N., Hostetler, J. L., and Norris, P. M., 2000, "Thermal Boundary Resistance Measurements Using a Transient Thermoreflectance Technique," Microsc. Thermophys. Eng., **4**(1), pp. 51–60.